Desalination and Water Treatment
www.deswater.com

doi: 10.5004/dwt.2023.29566

294 (2023) 202–212
May

Artificial neural network for modeling adsorption of ciprofloxacin onto Fe_3O_4/maifan stone composite

Shijie Chen[a,b,*], Nan Chen[a], Jinlong Li[a,b], Yan Zhuang[a], Guozhe Sui[a,b], Ying ying Huang[a,b], Huishu Zhang[a], Renjiang Lv[a,b], Guohua Dong[a,b], Dong xue Sun[a], Shuang Sui[a]

[a]*College of Chemistry and Chemical Engineering, Qiqihar University, Qiqihar 161006, China, Tel./Fax: +86-452-2742575; emails: csj060@163.com (S.J. Chen), chennan@qqhru.edu.cn (N. Chen), jinlong141@163.com (J.L. Li), 62777812@qq.com (Y. Zhuang), gzhsui@qqhru.edu.cn (G.Z. Sui), 402963101@qq.com (Y.Y. Huang), zhanghuishu0214@163.com (H.S. Zhang), lvrenjiang123@163.com (R.J. Lv), dongguohuaone@163.com (G.H. Dong), 2197716717@qq.com (D.X. Sun), 1739264271@qq.com (S. Sui)*
[b]*Heilongjiang Provincial Key Laboratory of Catalytic Synthesis for Fine Chemicals, Qiqihar University, Qiqihar 161006, China*

Received 31 December 2022; Accepted 17 April 2023

ABSTRACT

Novel Fe_3O_4/maifan stone composite were prepared by a simple solvothermal method. Physicochemical properties of the novel Fe_3O_4/maifan stone composite were analyzed using energy-dispersive X-ray spectroscopy, X-ray diffraction, scanning electron microscopy, transmission electron microscopy, N_2 adsorption, Fourier-transform infrared spectroscopy and X-ray photoelectron spectroscopy. The Fe_3O_4/maifan stone composite were used for the adsorption of ciprofloxacin (CIP) antibiotic removal. This paper represents an artificial neural network (ANN) based approach for modeling the adsorption process of the adsorption of CIP onto Fe_3O_4/maifan stone composite in batch adsorption experiments. The ANN model was trained and validated with the adsorption experiments data where pH, adsorbent dosage, and initial CIP concentration were selected as the variables for the batch study, whereas the removal efficiency was considered as the output. The ANN model was first developed using a three-layer back-propagation network with the optimum structure of 3-3-1. The model employed tangent sigmoid transfer function as input in the hidden layer whereas a linear transfer function was used in the output layer. The comparison between modeled data and experimental data provided high degree of correlation (R^2 = 0.99942) which indicated the applicability of ANN model for describing the adsorption process with reasonable accuracy. The kinetics of the adsorption of CIP onto Fe_3O_4/maifan stone composite was better fitted with the pseudo-second-order kinetics model, and thermodynamic parameters of the adsorption of CIP onto Fe_3O_4/maifan stone composite were calculated. This Fe_3O_4/maifan stone composite adsorbent can be easily separated.

Keywords: Adsorption; Fe_3O_4/maifan stone; Solvothermal; Artificial neural network (ANN) modeling; Ciprofloxacin

1. Introduction

Antibiotics are persistent in various water bodies due to ineffective biological degradation and are usually in an active state. It is possible to induce antibiotic resistance genes even in trace amounts in the environment [1–5].

Up to now, a variety of treatment technologies, such as biological treatment technology, advanced oxidation technology, photocatalytic degradation and so on, have been studied for the removal of antibiotics from environmental media [6–8]. In comparison, the advantages of adsorptive antibiotic removal technology are simple and economical [9–12].

According to relevant reports, the commonly used adsorption materials currently include natural mineral

* Corresponding author.

materials, synthetic metal oxides, and porous carbon materials [13–15]. In recent years, the removal of fluoroquinolones (FQs) antibiotics by adsorption has yet been reported. Biomass-based activated carbon, such as palm leaflets, *Trapa natans* husk removes FQs from aqueous environments [16–19]. Due to the high specific surface area and satisfactory pore controllability of the above-mentioned adsorption materials, they have attracted the interest of many researchers. However, these adsorption materials from micro- to nanoscale exhibit high implementation costs and low adsorption as well as easily being prone to secondary pollution of water, which limited their practical application [20].

The success of adsorption reactions greatly depends on the selection of absorbent materials [21–23]. Among the various adsorbent materials, magnetic adsorption materials are promising adsorbents for removing antibiotics owing to their high surface area and large pore volume [24–26]. Firstly, magnetic adsorption materials have received considerable attention due to their unique magnetic properties and potential applications in water treatment. Subsequently, maifan stones is a natural, non-toxic. The maifan stones has the advantages of large specific surface area, uniform pore-size distribution, good chemical stability and strong adsorption capacity, low cost and so on. For the convenient regeneration of the maifan stones from the aqueous solution, Fe_3O_4 are used to ensure the magnetism of maifan stones. All the advantages of Fe_3O_4/maifan stones as mentioned above suggested its great potential in improving the interfacial compatibility and adsorption capacity of Fe_3O_4/maifan stones.

Artificial neural network (ANN), as a major artificial intelligence tool with self-learning and adaptive capabilities, is commonly used to predict the removal process of pollutants in wastewater. ANN is composed of multiple artificial neurons and their connections, and a layered artificial neural network generally includes multiple hidden layers. The multilayer feed-forward net is a parallel interconnected structure consisting of input layer and includes independent variables, number of hidden layers, and output layer [27–32]. Adsorption methods have also widely applied ANN models in wastewater treatment modeling. Researchers have also conducted many studies using ANN models to reduce reagent dosage and energy input. Momina and Kafeel [33] employed ANN tool for the prediction of the behaviour of adsorption of Methyl orange using polyaniline/magnetic oxide nanocomposite. Fagundez et al. [34] reported a new methodology was proposed to fit the adsorption data of ions Ag^+, Cu^{2+}, and Co^{2+} onto zeolites Zeolite ZSM-5, Zeolite Y in its acid form (HY) and Zeolite 4a (4A), in four different temperatures. Ahmad et al. [35] represents an ANN based approach for modeling the adsorption process of sunset yellow onto neodymium modified order mesoporous carbon (OMC-Nd) in batch adsorption experiments [35]. Khandanlou et al. [36] represent the ANN modeling of adsorption of Pb(II) and Cu(II) was carried out for determination of the optimum values of the variables to get the maximum removal efficiency [36].

In the present study, the Fe_3O_4/maifan stone composite were prepared by a simple solvothermal method. The physiochemical properties of the novel Fe_3O_4/maifan stone composite were analyzed. Based on the experimental data obtained from batch adsorption experiments, a three-layer ANN model was applied to forecast the removal efficiency of ciprofloxacin (CIP) using Fe_3O_4/maifan stone composite as an adsorbent. To investigate the effects of the adsorption performance of the as-synthesized Fe_3O_4/maifan stone composite, the adsorption isotherm kinetics of CIP from aqueous solution on the Fe_3O_4/maifan stone were studied. The novel Fe_3O_4/maifan stone composite showed excellent magnetic response.

2. Experimental set-up

2.1. Materials

A standard product of ciprofloxacin was purchased from China National Institute for the Control the Pharmaceutical and Biological Products. Anhydrous ferric chloride ($FeCl_3$), glycol, anhydrous sodium acetate (CH_3COONa) were used as the starting materials. Other chemicals were of analytical grade.

2.2. Preparation of the Fe_3O_4/maifan stone composite

The schematic illustration of the preparation of the Fe_3O_4/maifan stone composite is shown as Fig. 1. $FeCl_3$ (1 mmol) were added into 80 mL glycol with strongly stirring followed by 0.5 h ultrasonication. Next, (1 mmol) CH_3COONa and 0.5 g maifan stone were added successively. The obtained solution was transferred into a Teflon sealed autoclave and maintained at 200°C for 8 h, The precipitate was collected and washed several times with distilled water and ethanol to remove any possible after drying at 60°C for 6 h.

2.3. Characterization

The sample crystallization behavior was examined using an X-ray diffraction meter using a Cu K_α radiation (λ = 0.15418 nm) (D/max-IIIA, Rigaku Corporation, Japan). The morphologies of the samples were characterized by scanning electron microscopy (SEM) and EDS spectrum were recorded with a field-emission scanning electron microscopy (Hitachi S-4300, Japan) with primary electron energy of 10 kV. Transmission electron microscopy were obtained with H-7650 (Hitachi, Japan). N_2 adsorption–desorption isotherms were measured using a chemisorption–physisorption analyzer (AUTOSORB-1, Kontakl Company,

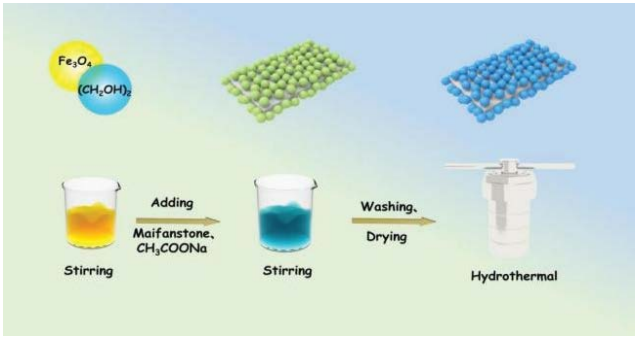

Fig. 1. Schematic illustration of the preparation of Fe_3O_4/maifan stone composite.

USA) at 77 K. The Fourier-transform infrared spectroscopy were recorded using a Fourier-transform infrared spectroscopy (FTIR) spectrometer (Nexus 670, Nicolet Co., Negoli Corporation of the United States).

2.4. Adsorptive removal

The adsorption of CIP on the Fe_3O_4/maifan stone composite were investigated at room temperature by adding 100 mg of Fe_3O_4/maifan stone composite into 200 mL CIP aqueous solution of different initial concentrations. The samples were continuously shaken for various contact times and were separated immediately by a magnet. The samples after filtration were analyzed by using a UV-Visible Spectrophotometer at 275 nm. The q_e (mg/g) of CIP at equilibrium, was calculated by the following equation:

$$q_e = \frac{(C_0 - C_e)V}{m} \quad (1)$$

where c_0 and c_e (mg/L) are the initial and equilibrium concentrations of CIP solution. V is the volume of the solution (L) and m is the weight of the adsorbent (g).

The kinetics experiment studies were performed following initial concentration of 10 mg/L, adsorbent dose (0.5 g/L) and initial pH of 6.5, and the samples were separated by a magnet at fixed time intervals. The q_t (mg/g) of CIP at time t, was calculated by the following equation:

$$q_t = \frac{(C_0 - C_t)V}{m} \quad (2)$$

where c_t is the concentration of the adsorbate mg/L in solution at time t.

3. Results and discussion

3.1. Characterization

The SEM image and transmission electron microscopy (TEM) image of the Fe_3O_4/maifan stone sample is shown in Fig. 2. It can be concluded that Fe_3O_4/maifan stone is composed of small nanospheres from SEM images (inset of Fig. 2a) and TEM images (inset of Fig. 2b).

The measurement results of chemical composition of the Fe_3O_4/maifan stone samples are shown in Fig. 3. The result shows the Fe_3O_4/maifan stone samples contained the C, O, Na, Mg, Al, Si, K, Ca and Fe elements. Fig. 4 shows the X-ray diffraction (XRD) patterns of the as-prepared the Fe_3O_4/maifan stone sample. The standard Fe_3O_4 structure is further confirmed by the splitting of the peaks at 2θ of 30°, 35°, 44°, 54°, 57° and 64°.

The nitrogen adsorption–desorption isotherms of the tested the Fe_3O_4/maifan stone materials presented in Fig. 5. The Fe_3O_4/maifan stone materials showed the isotherms of type IV and hysteresis loops of type H_3, which were related to their mesopores and macropores structure [37]. The average pore diameter about 161 nm suggests that the macropores are distributed very uniform. The Brunauer–Emmett–Teller (BET) specific surface area (S_{BET}) of Fe_3O_4/maifan

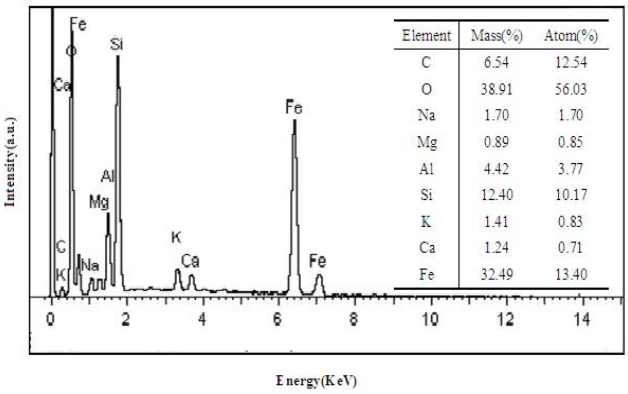

Element	Mass(%)	Atom(%)
C	6.54	12.54
O	38.91	56.03
Na	1.70	1.70
Mg	0.89	0.85
Al	4.42	3.77
Si	12.40	10.17
K	1.41	0.83
Ca	1.24	0.71
Fe	32.49	13.40

Fig. 3. Energy-dispersive X-ray spectrum of the Fe_3O_4/maifan stone sample.

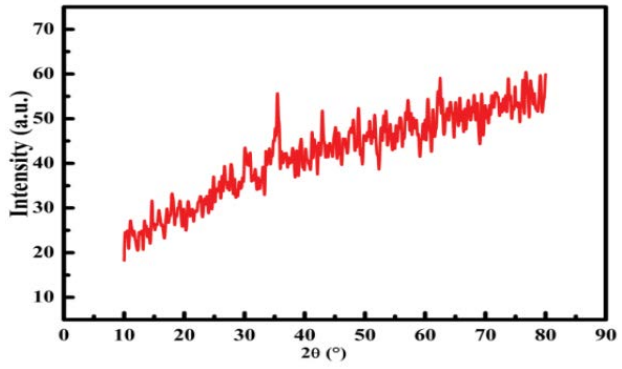

Fig. 4. The wide-angle X-ray diffraction patterns of the Fe_3O_4/maifan stone sample.

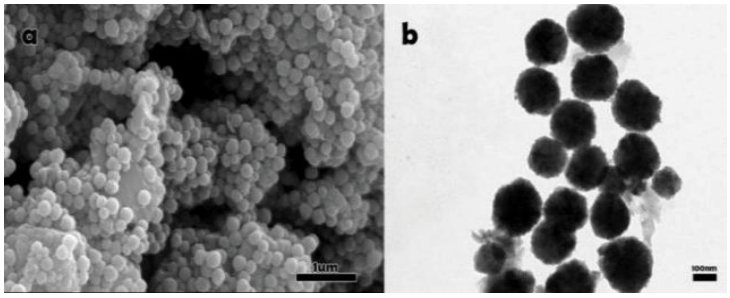

Fig. 2. Scanning and transmission electron microscopy image of Fe_3O_4/maifan stone.

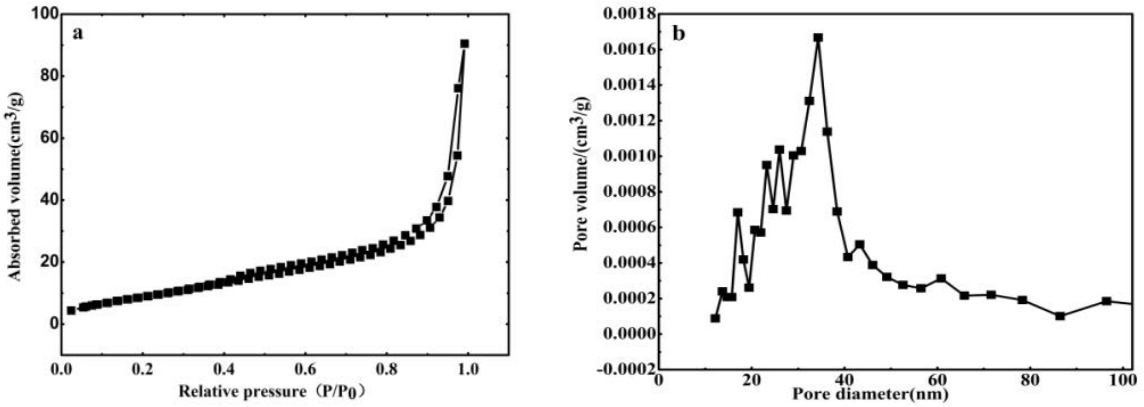

Fig. 5. Brunauer–Emmett–Teller surface area and pore-size distribution curves. (a) N_2 adsorption–desorption isotherms of the Fe_3O_4/maifan stone nanosheet composite. (b) Pore-size distribution of the Fe_3O_4/maifan stone nanosheet composite.

stone materials is as much as 34.86 m^2/g. The advantages of higher specific surface area and large void size of the Fe_3O_4/maifan stone will have a good prospects in the treatment of CIP for a magnetic adsorbent.

The chemical structures of Fe_3O_4/maifan stone samples were investigated using FTIR are shown in Fig. 6. The absorption peaks of the samples were observed at 3,393.42 and 1,630.26 cm^{-1}, which are ascribed to the bending and stretching vibrations by trace moisture [38]. The absorption bands of the Fe_3O_4/maifan stone at 1,042.06 cm^{-1} were attributed to Si–O–Si stretching mode of SiO_4, respectively. There are some differences in the three curves of Fe_3O_4/maifan stone sample at about 2,936.73 and 1,396.96 cm^{-1}, which may be attributed to the CO_2 existed in the sample. It is noteworthy that the bands at 585.37 and 434.08 cm^{-1} exhibited in the FTIR spectra of Fe_3O_4/maifan stone sample may be attributed to the vibrations of Si–O–Fe and Si–O–Si, O–Si–O bonds. This shows that Fe_3O_4 and maifan stone had formed complexes.

The X-ray photoelectron spectroscopy (XPS) analysis of the Fe_3O_4/maifan stone sample is performed in Fig. 7. As shown in Fig. 7a, the Fe_3O_4/maifan stone sample is composed of C, O, Na, Mg, Al, Si, K, Ca and Fe elements. the XPS of Fe 2p is shown in Fig. 7b, the peaks at 710.37, 712.05, 724.06 and 726.03 eV may correspond to Fe2p1/2 and Fe2p3/2, respectively [39,40]. In addition, the peak positions at 529.65 and 531.74 eV of O1s shown in Fig. 7c, respectively, suggest that there are two different O species [39].

The separation ability of Fe_3O_4/maifan stone sample are shown in Fig. 8. The magnetic Fe_3O_4/maifan stone materials were attracted by a magnet within 2 min, which indicated that the magnetic response of the synthesized material was good.

Fig. 9 shows the repeated adsorption capacity of Fe_3O_4/maifan stones under the same conditions. The adsorption capacity was set based on the first adsorption, and the subsequent adsorption capacity was calculated based on the first adsorption. After CIP was adsorbed, methanol was used as the eluents for CIP desorption. In the second round of CIP adsorption, the adsorption capacity of Fe_3O_4/maifan stones for CIP was about 90% of the first adsorption capacity. With an increase in the number of cycles to five, the adsorption capacity of Fe_3O_4/maifan stones to CIP was gradually decreased by 15%. Therefore, Fe_3O_4/maifan stones showed the satisfied advantage of repetitive absorption capacity for the CIP, which could have certain practical value in wastewater treatment.

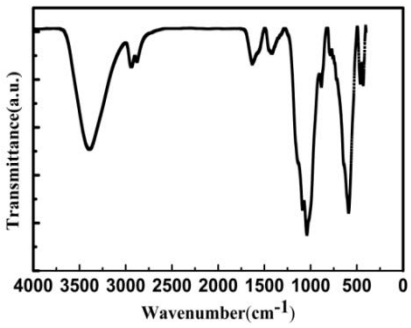

Fig. 6. Fourier-transform infrared spectra of the Fe_3O_4/maifan stone.

3.2. ANN modeling

The neural network of MATLAB 2013b mathematical software, was used to predict CIP adsorption removal. It is known that the number of its layers, the number of nodes in each layer and the nature of transfer functions determine the topology of an artificial neural network. In the present work, the initial pH, absorbent dose (g/L) and initial CIP concentration (mg/L) were the input variables given to the feed forward three-layered neural network. The removal efficiency was selected as output variable. The corresponding CIP removal was used as an output variable. Due to very large or small weights and to avoid numerical overflows, all inputs and target data were normalized between 0.1 and 0.9. The applied normalization equation is as follows:

$$y = 0.8\frac{x_i - x_{\min}}{x_{\max} - x_{\min}} + 0.1 \quad (3)$$

where y is the normalized value of x_i, $x_{\max}$ and $x_{\min}$ are respectively the maximum and minimum value of x_i. Fig. 10 displays the schematic illustration of the optimized ANN

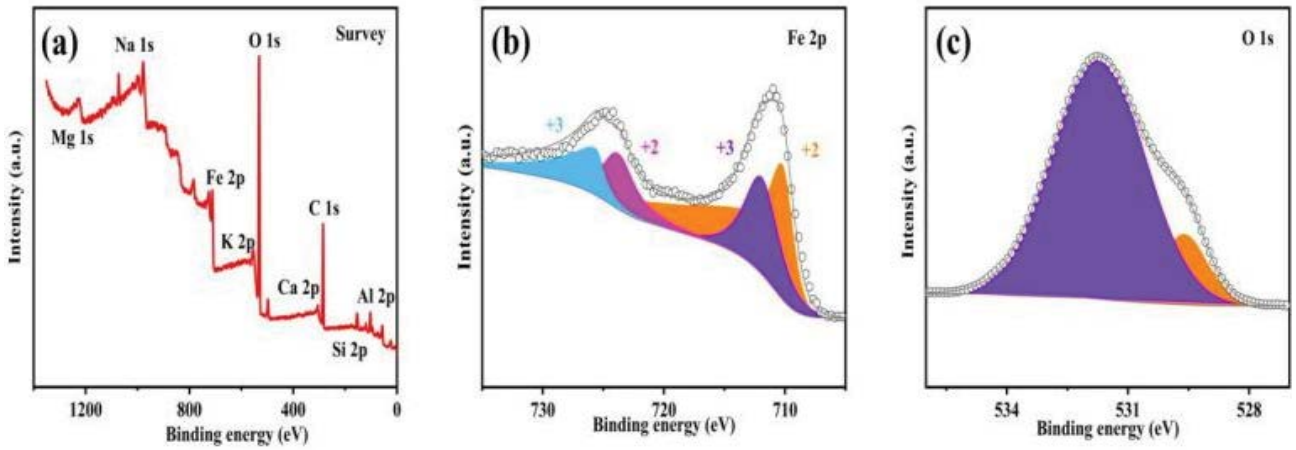

Fig. 7. X-ray photoelectron spectra of Fe_3O_4/maifan stone sample.

Fig. 8. Magnetism demonstration of Fe_3O_4/maifan stone.

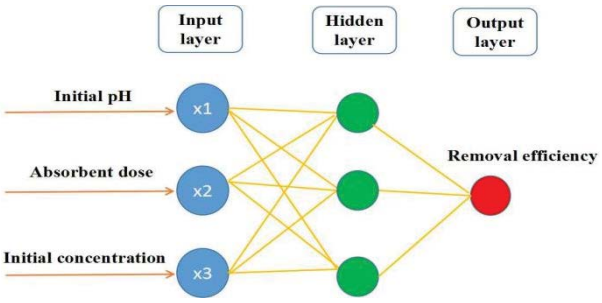

Fig. 10. A back-propagation artificial neural network schematic diagram.

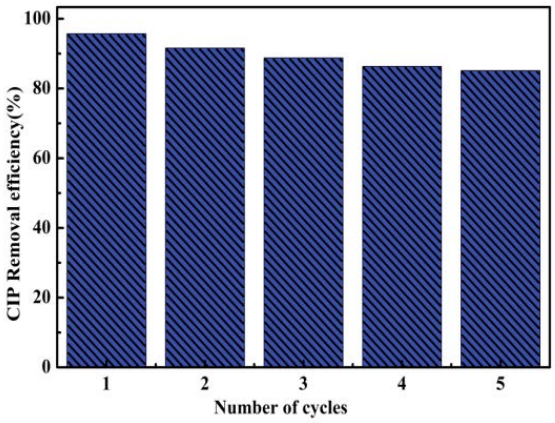

Fig. 9. Reuse of the Fe_3O_4/maifan stone or adsorption of ciprofloxacin.

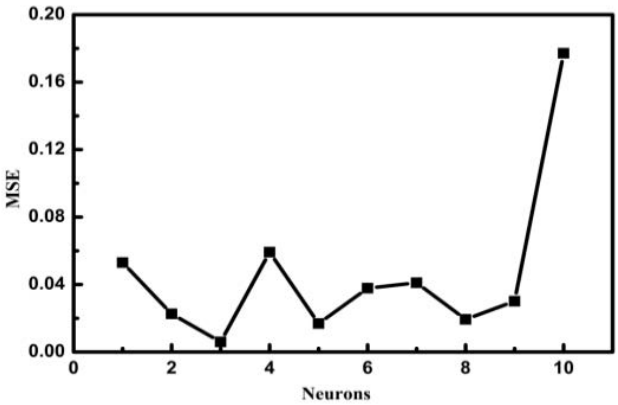

Fig. 11. Mean square error of neurons in the back-propagation artificial neural network model.

structure. Out of several data points generated, 17 experimental sets were employed to feed the ANN structure. The samples were divided into training, validation and test subsets, which contained 13, 2 and 2 samples, respectively. The mean square error (MSE), which was chosen as the function of error performance during the net training process, had the minimum value at 3 neurons among the examined neurons from 1 to 10. Due to the random initialization of the weights, each topology was repeated three times to avoid random correlation. Fig. 11 shows the relationship between the MSE and the number of neurons in the hidden layer. As can be seen, the lowest MSE was obtained with 3 neurons. Therefore, 3 neurons were found to represent the best performance of the neural network model. Fig. 12 shows the schematic illustration of the optimized ANN structure. The R^2 value (0.99942) of the back-propagation artificial neural network model indicates that the trained network performs accurately (Fig. 13). A comparison of the

experimental data and calculated values of the CIP removal efficiency is shown in Table 1. Table 2 shows the provided weights by ANN in the present study. The effect of each input variable on the output variable was calculated using the neural weight data. The influence for each input variable on the output variable was calculated by the Garson equation [Eq. (4)] using the weight (Table 3). Where I_j is the relative importance of the jth input variable on the output variable, N_i and N_h are respectively the numbers of input and hidden neurons, W_s are connection weights, the superscripts 'i', 'h' and 'o' refer respectively to input, hidden and output layers, and subscripts 'k', 'm' and 'n' refer respectively to input, hidden and output neurons. The results indicated that the absorbent dose (g/L) was the highest (51.6%), followed by initial CIP concentration (25.3%), and pH (23.1%). The impact of factors on the removal efficiency of CIP was also found to be in the following order: absorbent dose > initial CIP concentration > pH.

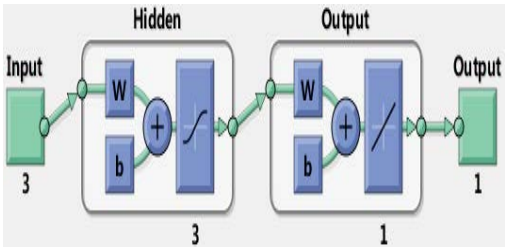

Fig. 12. Recommended artificial neural network structure.

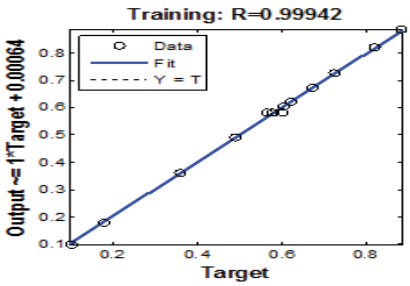

Fig. 13. Experimental and predicted data of normalized decontamination.

$$I_j = \frac{\sum_{m=1}^{m=N_h}\left(\left(\left|W_{jm}^{ih}\right| / \sum_{k=1}^{k=N_i}\left|W_{km}^{ih}\right|\right)\times\left|W_{mn}^{ho}\right|\right)}{\sum_{k=1}^{k=N_i}\left\{\sum_{m=1}^{m=N_h}\left(\left(\left|W_{jm}^{ih}\right| / \sum_{k=1}^{k=N_i}\left|W_{kn}^{ih}\right|\right)\times\left|W_{mm}^{ho}\right|\right)\right\}} \quad (4)$$

Table 2
Weights and biases of back-propagation artificial neural network in input-hidden layers (w_i and b_i) and hidden-output layer (w_j and b_j)

Neuron	w_{ih}		b_h	w_{ho}	b_o
1	–1.0422	0.1574	–1.2484	1.1494	0.8136	0.5089
2	1.3243	–3.6245	0.6465	0.8848	2.3437	
3	0.1416	3.1898	0.5099	–2.4320	2.6711	

Table 3
Relative influence of input variables

Input variables	Relative significance (%)	Order
Absorbent dose	51.6	1
Initial ciprofloxacin concentration	25.3	2
pH	23.1	3

Table 1
Comparison between predicted ciprofloxacin removal efficiency by the artificial neural network model and experimental values

Run	pH	Absorbent dose (g/L)	Ciprofloxacin (mg/L)	Actual value (%)	Predicted value (%)	ARD (%)
1	10.5	0.25	6	86.29	86.35	0.01
2	3.5	0.75	2	76.12	76.19	0.09
3	7	0.75	6	91.32	90.15	1.28
4	10.5	0.75	2	82.74	82.80	0.07
5	7	1.25	10	91.67	91.74	0.08
6	7	0.75	6	89.42	90.15	0.82
7	3.5	0.25	6	82.66	82.52	1.69
8	7	0.75	6	90.09	90.15	0.01
9	7	1.25	2	85.15	85.21	0.07
10	3.5	0.75	10	91.38	91.45	0.08
11	7	0.25	2	77.68	77.84	2.06
12	7	0.25	10	83.71	83.76	0.06
13	7	0.75	6	90.27	90.15	1.33
14	7	0.75	6	89.88	90.15	0.30
15	10.5	0.75	10	81.17	81.23	0.07
16	10.5	1.25	6	85.96	85.03	1.08
17	3.5	1.25	6	87.25	86.32	1.07

3.3. Adsorption studies

The adsorption ability of the Fe_3O_4/maifan stone from different initial concentrations of CIP (pH = 6.5) are demonstrated in Fig. 14. As can be seen, the Fe_3O_4/maifan stone showed higher adsorption capacities, which increased with the rise of the time. Thereafter, with the increase of time, the adsorption rate decreased gradually. The adsorption equilibrium was basically achieved within 90 min. At the initial concentrations of CIP of 5, 10, 20 and 40 mg/L, the removal rates of CIP were 97.4%, 95.7%, 94.9% and 93.9% within 150 min, respectively.

Fig. 15 shows the adsorption kinetics of CIP on the Fe_3O_4/maifan stone. The experimental kinetics data were fitted with pseudo-second-order models [41]:

$$\frac{t}{q_t} = \frac{1}{k_{ps} q_e^2} + \frac{t}{q_e} \tag{2}$$

where q_t is the amount of CIP adsorbed at time t (min), q_e is the amount of CIP adsorbed at equilibrium, k_{ps} is the constant of adsorption (g/mg·min). The parameters using pseudo-second-order models were calculated and presented in Table 4. According to the results, the pseudo-second-order model were demonstrated better fitting under four different concentrations CIP on the Fe_3O_4/maifan stone. The pseudo-second-order model has a higher R^2. The q_e derived from the pseudo-second-order model, and the actual situation differed significantly. As a result, the pseudo-second-order was better suited to describe Fe_3O_4/maifan stones adsorption behavior for CIP.

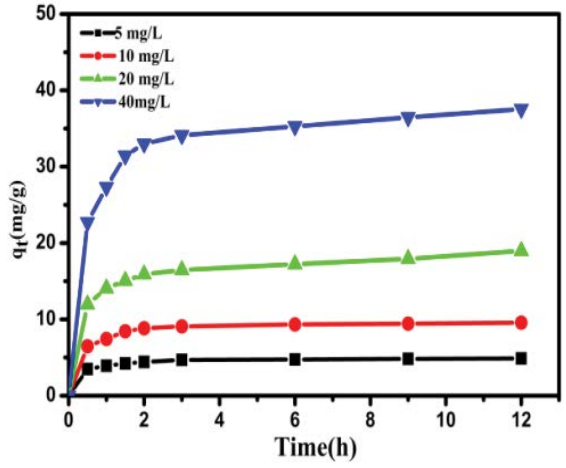

Fig. 14. Effect of contact time on the adsorption capacity of Fe_3O_4/maifan stone at different initial concentrations of ciprofloxacin.

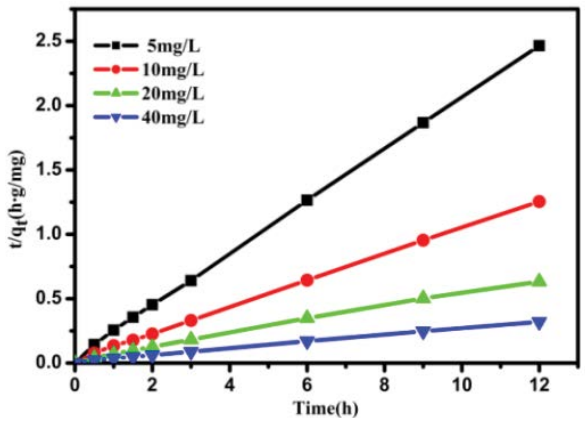

Fig. 15. Pseudo-second-order kinetics plots of ciprofloxacin adsorption on Fe_3O_4/maifan stone.

Fig. 16a shows the adsorption isotherm of CIP on Fe_3O_4/maifan stone (pH = 6.5)*f* or 12 h. The result showed that the amount of CIP on Fe_3O_4/maifan stone with the increase of the CIP concentration. Langmuir model was fitted with the experimental data of the adsorption isotherm of CIP on Fe_3O_4/maifan stone. Langmuir model can be written as:

$$\frac{C_e}{q_e} = \frac{C_e}{q_{max}} + \frac{1}{q_{max} K_L} \tag{5}$$

where c_e is the equilibrium concentration in liquid phase (mg/L), q_e is the equilibrium concentration on the solid phase (mg/g), q_{max} is the maximal adsorption capacity (73.8 mg/g) and K_L is affinity parameter related to the free energy of the adsorption (0.267 L/mg), respectively. The slope ($1/q_{max}$) and intercept ($1/q_{max}K_L$) of the linear plot are shown in Fig. 16b. Besides, the maximal adsorption CIP capacity of the Fe_3O_4/maifan stones were compared with the previously reported literature and displayed in Table 5. The adsorption isotherm is used to analyze the interaction between the adsorbent and the adsorbed molecule, as well as the adsorption properties. The R^2 of the models was higher than 0.90. It turns out that Langmuir model is fitted the result well. Based on the basic assumptions of the models, it could be deduced that the adsorption of CIP on the Fe_3O_4/maifan stones was monolayer.

In order to further understanding the adsorption behavior CIP on Fe_3O_4/maifan stone, the adsorption thermodynamics CIP on Fe_3O_4/maifan stone were investigated. Parameters including the Gibbs energy ($\Delta G°$), enthalpy ($\Delta H°$) and entropy ($\Delta S°$) changes are calculated according to the following equations [42]:

$$K_c = \frac{q_e}{C_e} \tag{6}$$

$$\Delta G° = -RT \ln K_c \tag{7}$$

Table 4
Adsorption kinetic parameters of ciprofloxacin adsorption on Fe_3O_4/maifan stone

Concentration of ciprofloxacin (mg/L)	q_e (mg/g)	k_{ps} (g/mg·h)	R^2
5	4.93	1.1000	0.9996
10	9.68	0.5312	0.9996
20	18.99	0.1562	0.9975
40	37.95	0.0904	0.9989

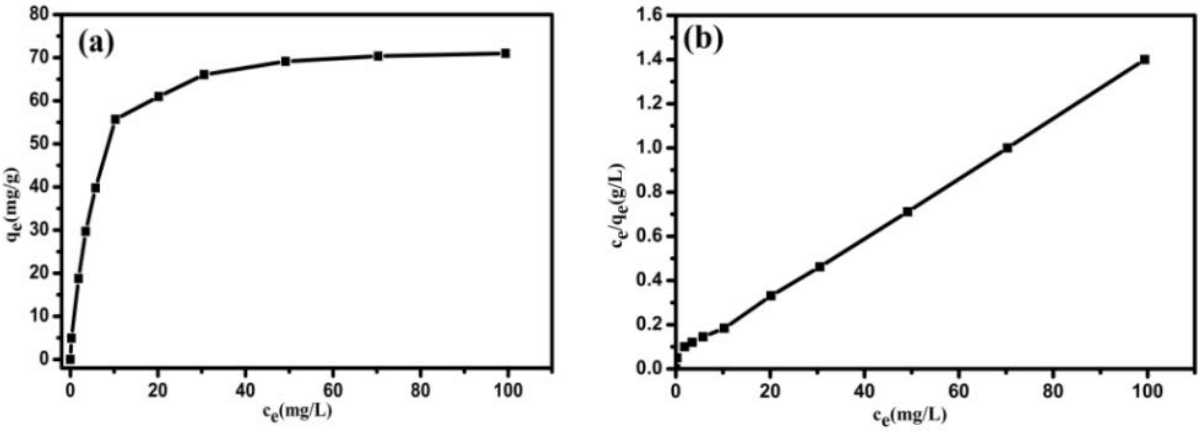

Fig. 16. Adsorption isotherm curve (a) and Langmuir plot of the isotherm (b) of Fe_3O_4/maifan stone.

Table 5
Comparison of ciprofloxacin adsorption capacity of Fe_3O_4/maifan stones with other ciprofloxacin reported in the literature

Formulation	Antibiotics	q_e (mg/g)	References
Fe_3O_4/maifan stones	Ciprofloxacin	73.8	This work
γ-Fe_2O_3/MFe_2O_4/CNTs	Ciprofloxacin	44.54	[21]
Aging PLA	Ciprofloxacin	1.256	[45]
Aging PE	Ciprofloxacin	0.9786	[45]
Aged biodegradable plastic PLA	Ciprofloxacin	46.913	[46]

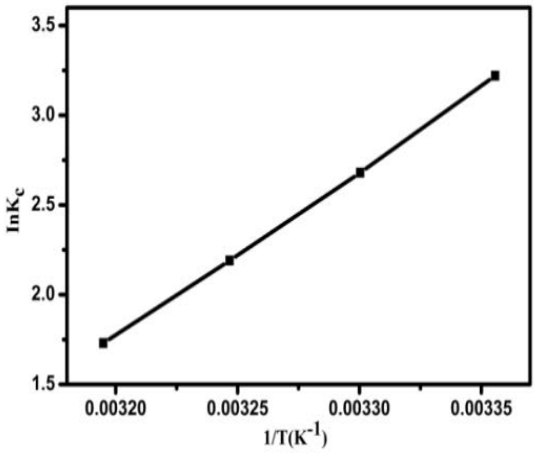

Fig. 17. A plot of lnK_c vs. 1/T.

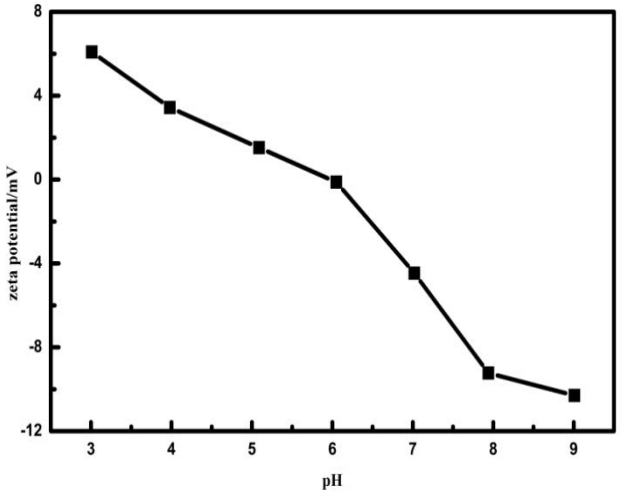

Fig. 18. Zeta potential of the Fe_3O_4/maifan stones.

Table 6
Thermodynamic parameters of ciprofloxacin adsorption on Fe_3O_4/maifan stone

Temperature (K)	ΔG° (kJ/mol)	ΔH° (kJ/mol)	ΔS° (J/mol·K)	R^2
298	2.897			
303	2.483	–76.96	–231.57	0.9995
308	2.007			
313	1.456			

$$\Delta G^\circ = \Delta H^\circ - T\Delta S^\circ \quad (8)$$

$$\ln K_c = \frac{\Delta S^\circ}{R} - \frac{\Delta H^\circ}{RT} \quad (9)$$

where K_c is the distribution coefficient, q_e and c_e are the equilibrium amount of CIP adsorbed on Fe_3O_4/maifan stone, and the equilibrium concentration of CIP in the solution, respectively, R is the gas constant (8.314 J/mol·K) and T is the temperature in Kelvin. ΔH° and ΔS° can be regarded as almost constant in temperature range (298 to 313 K) [37]. According to Eq. (7), the slope and intercept of the plot of lnK_c are plotted against 1/T is shown in Fig. 17. The adsorption thermodynamic parameters CIP on Fe_3O_4/maifan stone are listed in Table 6. These results suggested that the adsorption of CIP on the Fe_3O_4/maifan stones was an exothermic and spontaneous process. The low negative change of entropy values meant that the randomness on the interface

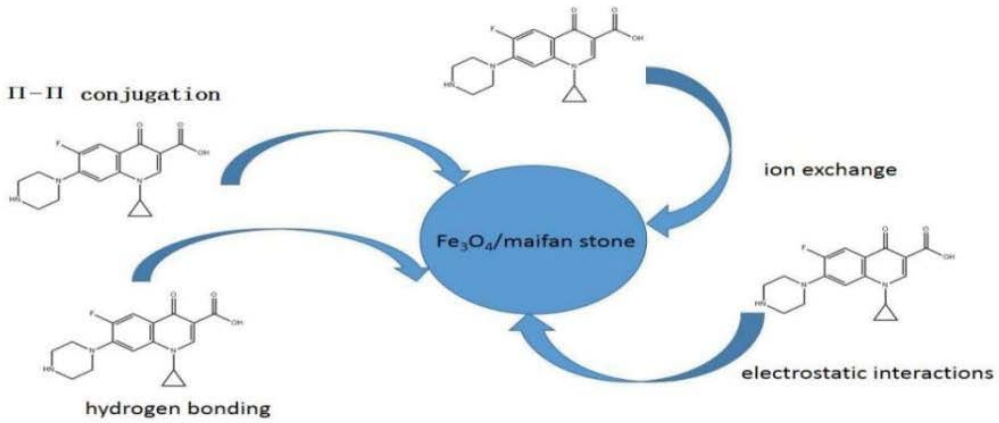

Fig. 19. Adsorption mechanisms.

of adsorbents decreased during the adsorption process. This suggested that the CIP adsorption the Fe_3O_4/maifan stones was controlled by physisorption [43].

It is fact that solution pH is an important factor influences he surface charge properties and the adsorption behavior of the Fe_3O_4/maifan stones. The pH-dependent adsorption of CIP on the Fe_3O_4/maifan stones could be reasonably explained by zeta potentials of the adsorbent combining with the dissociation state of CIP molecule in aqueous solution. As is shown in Fig. 18, the surface charge of as-prepared Fe_3O_4/maifan stone was highly dependent on solution pH and the point of zero charge (PZC) of Fe_3O_4/maifan stone was about 6.0. Therefore, below this pH, the particle surfaces were positively charged, and above this value, the particle surfaces were negative. In addition, CIP have proton-binding sites (carboxyl and piperazinyl group) with reported pK_{a1} (6.09) and pK_{a2} (8.74). At a pH of 6.5 between pK_{a1} (6.09) and pK_{a2} (8.74), the main species of CIP are zwitterions, which contain a positive charge and a negative charge concurrently, whereas the Fe_3O_4/maifan stones is negatively charged. That is, at pH < pH_{PZC} the adsorbent was positively charged due to the protonation of amino groups of chitosan and the positive charges increased with decreasing pH. Thus, the removal of CIP in this pH region was mainly attributed to the electrostatic attraction between positively charged adsorbent and negative groups of CIP. At pH > pH_{PZC}, the adsorbent was negatively charged ascribing to the deprotonation of amino groups of chitosan and the hydroxyl group of the Fe_3O_4/maifan stones. Thus the strong electrostatic repulsion between negative adsorbent and anionic CIP molecules as well as the competitive effect from hydroxyl ions would lead to decreased removal of CIP.

3.4. Adsorption mechanisms

Figs. 3, 6 and 7 show energy-dispersive X-ray spectroscopy (EDS), FTIR and XPS measurements to further elaborate the mechanism of CIP adsorption on the Fe_3O_4/maifan stone. The FTIR spectra in Fig. 6, reveal the intensity of O–H (3,393.42 cm^{-1}) and C=O (1,630.26 cm^{-1}) stretching vibration peaks showed a decreasing trend the Fe_3O_4/maifan stones, indicating that hydrogen bonding and π–π conjugate bonding played a vital role in adsorption [44]. The intensity of CH_2 (2,936.73 cm^{-1}), C–H (1,396.96 cm^{-1}), Si–O–Fe (585.37 cm^{-1}), Si–O–Si, O–Si–O (434.08 cm^{-1}) stretching vibration peaks increased after the adsorption of CIP for the Fe_3O_4/maifan stone, indicating that hydrogen bonding and π–π conjugate bonds determined their adsorption processes. The EDS and XPS spectra in Figs. 3 and 8 further reveal the mechanism of CIP adsorption by Fe_3O_4/maifan stone. The Fe_3O_4/maifan stone contains many kinds of metal ions, such as, Na^+, Mg^{2+}, Al^{3+}, K^+, Ca^{2+} and Fe^{2+} and Fe^{3+} etc. This observation suggests that ion exchange and electrostatic interactions are important in the mechanism of CIP adsorption by Fe_3O_4/maifan stone. In summary, the adsorption of CIP on Fe_3O_4/maifan stone is a mix of chemical and physical interactions. Chemical interactions included hydrogen conjugation, π–π bonding, and ion exchange. Electrostatic interactions and electrostatic repulsion were examples of physical interactions (Fig. 19).

4. Conclusions

The magnetically novel Fe_3O_4/maifan stone composite materials was successfully prepared by solvothermal method. Physicochemical properties of the novel Fe_3O_4/maifan stone composite were analyzed using EDS, XRD, SEM, TEM, N_2 adsorption, FTIR and XPS. The ANN model used a multilayer feedforward neural network consisting of one input layer with 3 neurons, one hidden layer with 3 neurons, and one output layer. The ANN model and experimental results showed similar patterns for all the parameters. The adsorption isotherm was best fitted with the Langmuir model employing a monolayer adsorption capacity of 73.8 mg/g. The results shows small nanospheres of the Fe_3O_4/maifan stone has good adsorption ability for CIP. Furthermore, Fe_3O_4/maifan stone have better magnetic separation ability.

Acknowledgments

This work has been supported by the Basic Research Business Special Fund of Heilongjiang Provincial Education Department (Research Project of Qiqihar University) (145109303), the higher education reform research project of Heilongjiang Provincial Education Department (SJGY20210939) and the Qiqihar University Education Science Research Program (GJQTYB202111).

References

[1] D.T. Jia, R.J. Zhang, J. Shao, W. Zhang, L.L. Cai, W.L. Sun, Exposure to trace levels of metals and fluoroquinolones increases inflammation and tumorigenesis risk of zebrafish embryos, Environ. Sci. Ecotechnol., 10 (2022) 100162, doi: 10.1016/j.ese.2022.100162.

[2] M. Ashfaq, K.N. Khan, S. Rasool, G. Mustafa, M. Saif-Ur-Rehman, M.F. Nazar, Q. Sun, C.-P. Yu, Occurrence and ecological risk assessment of fluoroquinolone antibiotics in hospital waste of Lahore, Pakistan, Environ. Toxicol. Pharmacol., 42 (2016) 16–22.

[3] N. Nakada, K. Kiri, H. Shinohara, A. Harada, K. Kuroda, S. Takizawa, H. Takada, Evaluation of pharmaceuticals and personal care products as water-soluble molecular markers of sewage, Environ. Sci. Technol., 42 (2008) 6347–6353.

[4] C.-P. Yu, K.-H. Chu, Occurrence of pharmaceuticals and personal care products along the West Prong Little Pigeon River in East Tennessee, USA, Chemosphere, 75 (2009) 1281–1286.

[5] C.L. Tong, X.J. Zhuo, Y. Guo, Occurrence and risk assessment of four typical fluoroquinolone antibiotics in raw and treated sewage and in receiving waters in Hangzhou, China, J. Agric. Food. Chem., 59 (2011) 7303–7309.

[6] S. Sekar, M. Surianarayanan, V. Ranganathan, D.R. MacFarlane, A.B. Mandal, Choline-based ionic liquids-enhanced biodegradation of azo dyes, Environ. Sci. Technol., 46 (2012) 4902–4908.

[7] Z.L. Li, J.S. Wang, J.J. Chang, B.M. Fu, H.T. Wang, Insight into advanced oxidation processes for the degradation of fluoroquinolone antibiotics: removal, mechanism, and influencing factors, Sci. Total Environ., 10 (2022) 159172, doi: 10.1016/j.scitotenv.2022.159172.

[8] T. Soltani, M.H. Entezari, Sono-synthesis of bismuth ferrite nanoparticles with high photocatalytic activity in degradation of Rhodamine B under solar light irradiation, Chem. Eng. J., 223 (2013) 145–154.

[9] Q. Liu, L.-B. Zhong, Q.-B. Zhao, C. Frear, Y.-M. Zheng, Synthesis of Fe_3O_4/polyacrylonitrile composite electrospun nanofiber Mat for effective adsorption of tetracycline, ACS Appl. Mater. Interfaces, 7 (2015) 14573−14583.

[10] A. Gómez-Avilés, L. Sellaoui, M. Badawi, A. Bonilla-Petriciolet, J. Bedia, C. Belver, Simultaneous adsorption of acetaminophen, diclofenac and tetracycline by organo-sepiolite: experiments and statistical physics modelling, Chem. Eng. J., 404 (2021) 126601, doi: 10.1016/j.cej.2020.126601.

[11] Y. Wang, X.J. Wang, Y. Li, J. Li, Y.Y. Liu, S.Q. Xia, J.F. Zhao, Effects of exposure of polyethylene microplastics to air, water and soil on their adsorption behaviors for copper and tetracycline, Chem. Eng. J., 404 (2020) 126412, doi: 10.1016/j.cej.2020.126412.

[12] M.J. Ahmed, S.K. Theydan, Fluoroquinolones antibiotics adsorption onto microporous activated carbon from lignocellulosic biomass by microwave pyrolysis, J. Taiwan Inst. Chem. Eng., 45 (2014) 219–226.

[13] Y.P. Li, C.F. Zeng, C.Q. Wang, L.X. Zhang, Preparation of C@silica core/shell nanoparticles from ZIF-8 for efficient ciprofloxacin adsorption, Chem. Eng. J., 343 (2018) 645–653.

[14] J.J. Zhang, X.L. Yan, X.Y. Hu, R. Feng, M. Zhou, Direct carbonization of Zn/Co zeolitic imidazolate frameworks for efficient adsorption of Rhodamine B, Chem. Eng. J., 347 (2018) 640–647.

[15] L. Joseph, B.-M. Jun, M. Jang, C.M. Park, J.C. Muñoz-Senmache, A.J. Hernández-Maldonado, A. Heyden, M. Yu, Y.M. Yoon, Removal of contaminants of emerging concern by metal–organic framework nanoadsorbents: a review, Chem. Eng. J., 369 (2019) 928–946.

[16] R.M. Rego, G. Kuriya, M.D. Kurkuri, M. Kigga, MOF based engineered materials in water remediation: recent trends, J. Hazard. Mater., 403 (2021) 123605, doi: 10.1016/j.jhazmat.2020.123605.

[17] E.-S.I. El-Shafey, H. Al-Lawati, A.S. Al-Sumri, Ciprofloxacin adsorption from aqueous solution onto chemically prepared carbon from date palm leaflets, J. Environ. Sci., 24 (2012) 1579–1586.

[18] S.A.C. Carabineiro, T. Thavorn-amornsri, M.F.R. Pereira, J.L. Figueiredo, Adsorption of ciprofloxacin on surface-modified carbon materials, Water Res., 45 (2011) 4583–4591.

[19] W.F. Liu, J. Zhang, C.L. Zhang, L. Ren, Sorption of norfloxacin by lotus stalk-based activated carbon and iron-doped activated alumina: mechanisms, isotherms and kinetics, Chem. Eng. J., 171 (2011) 431–438.

[20] J.A. González, J.G. Bafico, M.E. Villanueva, S.A. Giorgieri, G.J. Copello, Continuous flow adsorption of ciprofloxacin by using a nanostructured chitin/graphene oxide hybrid material, Carbohydr. Polym., 188 (2018) 213–220.

[21] J.J. Yao, Y. Deng, D.-S. Li, H.P. Li, H.Y. Yang, Role of magnetic substances in adsorption removal of ciprofloxacin by gamma ferric oxide and ferrites co-modified carbon nanotubes, J. Colloid Interface Sci., 638 (2023) 872–881.

[22] D. Yang, M. Du, Z.-u. Din, S.K. Yang, L. Chen, J. Cai, J. Pang, X. Chen, W.P. Ding, Synthesis and ciprofloxacin adsorption of Gum Ghatti/Konjac Glucomannan/Zif-8 composite aerogel, Colloids Surf., A, 664 (2023) 131196, doi: 10.1016/j.colsurfa.2023.131196.

[23] C. Liu, M.Q. Zhao, S.Y. He, Z. Cao, W. Chen, Fe_3O_4 magnetic nanoparticles as a catalyst of oxone for the removal of a typical amino acid, Desal. Water Treat., 97 (2017) 262–271.

[24] S. Shi, Y.W. Fan, Y.M. Huang, Facile low temperature hydrothermal synthesis of magnetic mesoporous carbon nanocomposite for adsorption removal of ciprofloxacin antibiotics, Ind. Eng. Chem. Res., 52 (2013) 2604–2612.

[25] H.J. Wu, H.L. Zhang, W.J. Zhang, X.F. Yang, H. Zhou, Z.Q. Pan, D.S. Wang, Preparation of magnetic polyimide@Mg-Fe layered double hydroxides core-shell composite for effective removal of various organic contaminants from aqueous solution, Chemosphere, 219 (2019) 66–75.

[26] Ö. Kerkez-Kuyumcu, Ş.S. Bayazit, M. Abdel Salam, Antibiotic amoxicillin removal from aqueous solution using magnetically modified graphene nanoplatelets, J. Ind. Eng. Chem., 36 (2016) 198–205.

[27] K.L. Bhowmik, A. Debnath, R.K. Nath, B. Saha, Synthesis of $MnFe_2O_4$ and Mn_3O_4 magnetic nano-composites with enhanced properties for adsorption of Cr(VI): artificial neural network modeling, Water Sci. Technol., 76 (2017) 3368–3378.

[28] A. Deb, M. Kanmani, A. Debnath, K.L. Bhowmik, B. Saha, Preparation and characterization of magnetic $CaFe_2O_4$ nanoparticles for efficient adsorption of toxic Congo red dye from aqueous solution: predictive modeling by artificial neural network, Desal. Water Treat., 89 (2017) 197–209.

[29] K.L. Bhowmik, A. Debnath, R.K. Nath, S. Das, K.K. Chattopadhyay, B. Saha, Synthesis and characterization of mixed phase manganese ferrite and hausmannite magnetic nanoparticle as potential adsorbent for methyl orange from aqueous media: artificial neural network modeling, J. Mol. Liq., 219 (2016) 1010–1022.

[30] I. Ghosh, S. Kar, T. Chatterjee, N. Bar, S.K. Das, Removal of methylene blue from aqueous solution using *Lathyrus sativus* husk: adsorption study, MPR and ANN modelling, Process Saf. Environ. Prot., 149 (2021) 345–361.

[31] M. Zahedinejad, N. Sohrabi, R. Mohammadi, Magnetic multi-walled carbon nanotubes as an efficient sorbent for pirimicarb removal from aqueous solutions in continuous (FBAC) and batch formats: thermodynamic, kinetic, isotherm study, optimization and modeling by RSM-ANN, J. Mol. Liq., 370 (2023) 120915, doi: 10.1016/j.molliq.2022.120915.

[32] J.L.S. Fagundez, M.S. Netto, G.L. Dotto, N.P.G. Salau, A new method of developing ANN-isotherm hybrid models for the determination of thermodynamic parameters in the adsorption of ions Ag^+, Co^{2+} and Cu^{2+} onto zeolites ZSM-5, HY, and 4A, J. Environ. Chem. Eng., 9 (2021) 106126, doi: 10.1016/j.jece.2021.106126.

[33] Momina, A. Kafeel, Remediation of anionic dye from aqueous solution through adsorption on polyaniline/FO nanocomposite-modelling by artificial neural network (ANN), J. Mol. Liq., 360 (2022) 119497, doi: 10.1016/j.molliq.2022.119497.

[34] J.L.S. Fagundez, M.S. Netto, G.L. Dotto, N.P.G. Salau, A new method of developing ANN-isotherm hybrid models for the

determination of thermodynamic parameters in the adsorption of ions Ag^{+}, Co^{2+} and Cu^{2+} onto zeolites ZSM-5, HY, and 4A, J. Environ. Chem. Eng., 9 (2021) 106126, doi: 10.1016/j.jece.2021.106126.

[35] Z.U. Ahmad, L.G. Yao, Q.Y. Lian, F. Islam, M.E. Zappi, D.D. Gang, The use of artificial neural network (ANN) for modeling adsorption of sunset yellow onto neodymium modified ordered mesoporous carbon, Chemosphere, 256 (2020) 127081, doi: 10.1016/j.chemosphere.2020.127081.

[36] R. Khandanlou, H.R.F. Masoumi, M.B. Ahmad, K. Shameli, M. Basri, K. Kalantari, Enhancement of heavy metals sorption via nanocomposites of rice straw and Fe_3O_4 nanoparticles using artificial neural network (ANN), Ecol. Eng., 91 (2016) 249–256.

[37] Y.F. Zhu, E. Kockrick, T. Ikoma, N. Hanagata, S. Kaskel, An efficient route to rattle-type Fe_3O_4@SiO_2 hollow mesoporous spheres using colloidal carbon spheres templates, Chem. Mater., 21 (2009) 2547–2553.

[38] F.Y.K. Wang, Y.L. Tang, B.B. Zhang, B.D. Chen, Y.L. Wang, Preparation of novel magnetic hollow mesoporous silica microspheres and their efficient adsorption, J. Colloid Interface Sci., 386 (2012) 129–134.

[39] S.Q. Jiao, M.Z. Wu, X.X. Yu, H. Zhang, Enhanced microwave absorption: the composite of Fe_3O_4 flakes and reduced graphene oxide with improved interfacial polarization, Adv. Eng. Mater., 22 (2020) 1901299, doi: 10.1002/adem.201901299.

[40] S.B. Huang, W.X. Zhang, S.Z. Cui, W.T. Wei, W.H. Chen, L.W. Mi, Large–scale uniform 3D composite Fe_3O_4@CF for high–performance supercapacitors design, ChemistrySelect, 1 (2016) 2909.

[41] V. Vadivelan, K. Vasanth Kumar, Equilibrium, kinetics, mechanism, and process design for the sorption of methylene blue onto rice husk, J. Colloid Interface Sci., 286 (2005) 90–100.

[42] L.J. You, Z.J. Wu, T.H. Kim, K.T. Lee, Kinetics and thermodynamics of bromophenol blue adsorption by a mesoporous hybrid gel derived from tetraethoxysilane and bis(trimethoxysilyl)hexane, J. Colloid Interface Sci., 300 (2006) 526–535.

[43] R.A. Reza, M. Ahmaruzzaman, A novel synthesis of Fe_2O_3@ activated carbon composite and its exploitation for the elimination of carcinogenic textile dye from an aqueous phase, RSC Adv., 5 (2015) 10575–10586.

[44] Y.C. Xiong, J.H. Zhao, L.Q. Li, Y.Y. Wang, X.H. Dai, F. Yu, J. Ma, Interfacial interaction between micro/nanoplastics and typical PPCPs and nanoplastics removal via electrosorption from an aqueous solution, Water Res., 184 (2020) 116100, doi: 10.1016/j.watres.2020.116100.

[45] J.N. Liang, J.H. Wu, Z. Zeng, M.Z. Li, W.Z. Liu, T.P. Zhang, Behavior and mechanisms of ciprofloxacin adsorption on aged polylactic acid and polyethlene microplastics, Environ. Sci. Pollut. Res., 30 (2023) 62938–62950.

[46] M.H. Zheng, P.W. Wu, L.Q. Li, F. Yu, J. Ma, Adsorption/desorption behavior of ciprofloxacin on aged biodegradable plastic PLA under different exposure conditions, J. Environ. Chem. Eng., 11 (2023) 109256, doi: 10.1016/j.jece.2022.109256.